GEOPHYSICS, VOL. 71, NO. 6 (NOVEMBER-DECEMBER 2006); P. S261–S272, 18 FIGS.
10.1190/1.2357832

Plane-wave depth migration

Paul L. Stoffa[1], Mrinal K. Sen[1], Roustam K. Seifoullaev[2], Reynam C. Pestana[3], and Jacob T. Fokkema[4]

ABSTRACT

We present fast and efficient plane-wave migration methods for densely sampled seismic data in both the source and receiver domains. The methods are based on slant stacking over both shot and receiver positions (or offsets) for all the recorded data. If the data-acquisition geometry permits, both inline and crossline source and receiver positions can be incorporated into a multidimensional phase-velocity space, which is regular even for randomly positioned input data. By noting the maximum time dips present in the shot and receiver gathers and constant-offset sections, the number of plane waves required can be estimated, and this generally results in a reduction of the data volume used for migration. The required traveltime computations for depth imaging are independent for each particular plane-wave component. It thus can be used for either the source or the receiver plane waves during extrapolation in phase space, reducing considerably the computational burden. Since only vertical delay times are required, many traveltime techniques can be employed, and the problems with multipathing and first arrivals are either reduced or eliminated. Further, the plane-wave integrals can be pruned to concentrate the image on selected targets. In this way, the computation time can be further reduced, and the technique lends itself naturally to a velocity-modeling scheme where, for example, horizontal and then steeply dipping events are gradually introduced into the velocity analysis. The migration method also lends itself to imaging in anisotropic media because phase space is the natural domain for such an analysis.

INTRODUCTION

Depth migration is used to recover subsurface images from seismic data recorded at the surface. Poststack and prestack migration methods have been developed and used in various domains (space-time, space-frequency, wavenumber-frequency, etc.) and include such classical methods as Kirchhoff-integral migration (Schneider, 1978), migration in the *f-k* domain (Stolt, 1978), and reverse-time migration in the *x-t* domain (McMechan, 1983).

Recently, plane-wave-based methods have been investigated for migration (Hildebrand and Carroll, 1993; Akbar et al., 1996; Romero et al., 2000; Liu et al., 2002). Plane-wave decomposition or slant stacking converts the surface-recorded $\mathbf{x}$-t seismic data to the intercept time τ and ray parameter $\mathbf{p}$. For marine data, each ray parameter corresponds to a particular angle of incidence for the seismic data recorded on the surface. This τ-$\mathbf{p}$ transformation offers numerous advantages for processing and interpretation of data: τ-$\mathbf{p}$ filtering to enhance or eliminate specific seismic waves (Tatham, 1989); velocity-analysis methods that are not dependent on the small angle of incidence approximation (Schultz and Claerbout, 1978; Diebold and Stoffa, 1981); direct inversion of plane-wave seismic data (Sen and Stoffa, 1991; Xia et al., 1998); and multiples suppression (Liu et al., 2000). Modern seismic data have adequate spatial sampling and sufficient aperture to avoid artifacts and edge effects and produce high-quality τ-$\mathbf{p}$ data for plane-wave processing and imaging.

Plane-wave migration methods use data transformed to the τ-$\mathbf{p}$ domain; an appropriate extrapolation operator is then designed to continue the wavefield (characterized by its surface-ray parameter) downward in depth. For example, Akbar et al. (1996) used plane-wave and point-source traveltimes for this purpose. Gaussian-beam

Manuscript received by the Editor January 9, 2006; revised manuscript received May 11, 2006; published online October 31, 2006.
[1]University of Texas at Austin, Institute for Geophysics, 4412 Spicewood Springs Road, Building 600, Austin, Texas 78759 and University of Texas at Austin, Department of Geological Sciences, 1 University Station, C1100, Austin, Texas 78712. E-mail: pauls@ig.utexas.edu; mrinal@ig.utexas.edu
[2]University of Texas at Austin, Institute for Geophysics, 4412 Spicewood Springs Road, Building 600, Austin, Texas 78759. E-mail: roustam@ig.utexas.edu
[3]Universidade Federal da Bahia, Instituto de Geosciências, Campus Universitário da Federaçao, Salvador, Bahia, Brazil.
[4]Delft University of Technology, Delft, the Netherlands.

methods originally proposed to compute wavefields in heterogeneous media (Popov, 1982) do not break at caustics. This property has been exploited in Gaussian-beam migration by Hill (1990). However, Hill's (1990) Gaussian-beam migration makes use of locally slant-stacked traces, which are extrapolated using beams. In other words, the plane-wave components are expressed as an expansion in terms of Gaussian beams (Popov, 1982; Nowack et al., 2003, 2006).

In this paper, we consider depth-migration methods based on one or more plane-wave decompositions of the original seismic data. With the aid of asymptotic ray theory (ART), plane-wave methods are developed that handle arbitrary velocity structures without any dip limitations. Alternatively, the extrapolation operator can be derived by using Maslov Green's function in the scattering integral. The Maslov-Born method has been used in migration by Xu (1998). However, our approach differs substantially from all these existing techniques in that we employ a double downward-continuation formulation (Clayton and Stolt, 1981; Stolt and Weglein, 1985; Hildebrand and Carroll, 1993) for seismic data recorded at the surface. To develop plane-wave depth-migration algorithms (for receiver plane waves, source plane waves, both source and receiver plane waves, and offset plane waves), we use the ART approximation for both Green's functions and decompose the seismic data into one or more desired plane-wave components via slant stacking, which we discuss first.

Note that our plane-wave-based migration methods can easily include anisotropy, using, for example, the delay-time computation methods described in Sen and Mukherjee (2003) and Faria and Stoffa (1994).

SLANT STACK

A detailed description of the τ-$\mathbf{p}$ transformation can be found in Claerbout (1976), Stoffa et al. (1981), Brysk and McCowan (1986), Stoffa (1989), and Foster and Mosher (1992). The slant stack of the wavefield $U(\mathbf{x},t)$ recorded at the surface location $\mathbf{x}$ at time t is defined as

$$\hat{U}(\mathbf{p},\tau) = \int U(\mathbf{x},\tau + \mathbf{p}\cdot\mathbf{x})d\mathbf{x} \tag{1}$$

and, in effect, is the summation of seismic data along linear $\mathbf{x}$-t traveltime trajectories corresponding to planes of apparent horizontal slowness or ray parameter $\mathbf{p}$. This transformation is linear and can be inverted:

$$U(\mathbf{x},t) = \rho * \int \hat{U}(\mathbf{p},t - \mathbf{p}\cdot\mathbf{x})d\mathbf{p}, \tag{2}$$

where * is convolution and $\rho(t)$ in the frequency domain is the filter ω^2, where ω is the angular frequency.

In practice, the τ-$\mathbf{p}$ transformation in the space-time domain requires two steps: first, a linear moveout for the plane wave with ray parameter $\mathbf{p}$ performed by applying the time shift for a particular slant and then the data summed over all recorded offsets to obtain the transformed data. Repeating this slant-stacking procedure for a range of $\mathbf{p}$ values generates a τ-$\mathbf{p}$ gather. Each trace of the resulting τ-$\mathbf{p}$ transformed data estimates the plane-wave arrivals at different angles of incidence on the surface as recorded by the receivers; see, for example, Figure 3 of Diebold and Stoffa (1981).

Typically, the τ-$\mathbf{p}$ transformation is performed for a fixed-source position $\mathbf{s}$ (that is, with respect to the receivers with their offsets $\mathbf{o}$, relative to the source position). Given modern multicoverage data $P(\mathbf{s},\mathbf{r},t)$, where $\mathbf{r}$ is the receiver location, there is no practical reason nor obstacle not to apply the τ-$\mathbf{p}$ transformation with respect to $\mathbf{r}$ or $\mathbf{s}$, or even both (Stoffa et al., 2005).

In the frequency domain, the decomposition of the recorded data $P(\mathbf{s},\mathbf{r},\omega)$ into plane-wave components is accomplished using a variant of slant stacking. Usually, this involves applying a phase shift to each trace with respect to its shot position (Schultz and Claerbout, 1978; Stoffa et al., 1981). For each fixed-source position, we transform the recorded data by summing over all the receiver positions relative to the source position (i.e., the offsets) using

$$P(\mathbf{s},\mathbf{p_o},\omega) = \int P(\mathbf{s},\mathbf{o},\omega)\exp(+\,i\omega\mathbf{p_o}\cdot\mathbf{o})d\mathbf{o}, \tag{3}$$

where $P(\mathbf{s},\mathbf{p_o},\omega)$ represents the typical plane-wave data with ray parameter $\mathbf{p_o}$ and the argument $\mathbf{o} = \mathbf{r} - \mathbf{s}$ is the signed source-receiver offset.

In the frequency domain, the slant stack can be viewed as a Fourier transform with $\mathbf{k} = \omega\mathbf{p_o}$. Then the inverse slant stack is given by

$$P(\mathbf{s},\mathbf{o},\omega) = \omega^2 \int P(\mathbf{s},\mathbf{p_o},\omega)\exp(-\,i\omega\mathbf{p_o}\cdot\mathbf{o})d\mathbf{p_o}. \tag{4}$$

Since we are also interested in developing imaging algorithms relative to the absolute survey positions $\mathbf{s}$ and $\mathbf{r}$, we use the following variant of the forward and inverse slant-stacking formulas:

$$P(\mathbf{s},\mathbf{p_r},\omega) = \int P(\mathbf{s},\mathbf{r},\omega)\exp(+\,i\omega\mathbf{p_r}\cdot\mathbf{r})d\mathbf{r}, \tag{5}$$

$$P(\mathbf{s},\mathbf{r},\omega) = \omega^2 \int P(\mathbf{s},\mathbf{p_r},\omega)\exp(-\,i\omega\mathbf{p_r}\cdot\mathbf{r})d\mathbf{p_r}. \tag{6}$$

Here, $P(\mathbf{s},\mathbf{p_r},\omega)$ represents the plane-wave data with respect to the absolute source position $\mathbf{s}$, and we assume that the survey origin is at $(0.,0.,0.)$.

Similarly, for each receiver gather, i.e., for fixed-receiver position $\mathbf{r}$, the data may be transformed into plane waves by summing over all source positions as

$$P(\mathbf{p_s},\mathbf{r},\omega) = \int P(\mathbf{s},\mathbf{r},\omega)\exp(+\,i\omega\mathbf{p_s}\cdot\mathbf{s})d\mathbf{s}. \tag{7}$$

The inverse slant stack is given by

$$P(\mathbf{s},\mathbf{r},\omega) = \omega^2 \int P(\mathbf{p_s},\mathbf{r},\omega)\exp(-\,i\omega\mathbf{p_s}\cdot\mathbf{s})d\mathbf{p_s}. \tag{8}$$

Here, $P(\mathbf{p_s},\mathbf{r},\omega)$ represents the plane-wave data registered with respect to the absolute receiver position $\mathbf{r}$.

Finally, the above variant of slant stacking can be applied to decompose all recorded source and receiver data simultaneously into plane waves using

$$P(\mathbf{p_s},\mathbf{p_r},\omega) = \iint P(\mathbf{s},\mathbf{r},\omega) \times \exp(+\,i\omega[\mathbf{p_r}\cdot\mathbf{r} + \mathbf{p_s}\cdot\mathbf{s}])d\mathbf{s}d\mathbf{r}, \quad (9)$$

with the inverse slant stack given by

$$P(\mathbf{s},\mathbf{r},\omega) = \omega^4 \iint P(\mathbf{p_s},\mathbf{p_r},\omega) \times \exp(-\,i\omega[\mathbf{p_r}\cdot\mathbf{r} + \mathbf{p_s}\cdot\mathbf{s}])d\mathbf{p_s}d\mathbf{p_r}, \quad (10)$$

or in terms of offset $\mathbf{o} = \mathbf{r} - \mathbf{s}$, using

$$P(\mathbf{p_s},\mathbf{p_o},\omega) = \iint P(\mathbf{s},\mathbf{o},\omega) \times \exp(+\,i\omega[\mathbf{p_o}\cdot\mathbf{o} + \mathbf{p_s}\cdot\mathbf{s}])d\mathbf{s}d\mathbf{o}, \quad (11)$$

with the inverse slant stack given by

$$P(\mathbf{s},\mathbf{o},\omega) = \omega^4 \iint P(\mathbf{p_s},\mathbf{p_o},\omega) \times\exp(-\,i\omega[\mathbf{p_o}\cdot\mathbf{o} + \mathbf{p_s}\cdot\mathbf{s}])d\mathbf{p_s}d\mathbf{p_o}. \quad (12)$$

DOUBLE DOWNWARD-CONTINUATION INTEGRAL

In the frequency domain, the double downward-continuation integral (Clayton and Stolt, 1981; Stolt and Weglein, 1985; Hildebrand and Carroll, 1993) for wavefield continuation of sources and receivers to depth is

$$P(\mathbf{x},\omega) = \int \partial_n G(\mathbf{x},\mathbf{s},\omega)d\mathbf{s} \int \partial_n G(\mathbf{x},\mathbf{r},\omega)P(\mathbf{s},\mathbf{r},\omega)d\mathbf{r}, \quad (13)$$

where $P(\mathbf{s},\mathbf{r},\omega)$ is the seismic wavefield measured at the surface, G is the Green's function, $\partial_n G$ is the surface normal derivative of the Green's function, $\mathbf{x}$ is the subsurface location, and $P(\mathbf{x},\omega)$ is the predicted wavefield at depth.

To extrapolate the measured seismic wavefield $P(\mathbf{s},\mathbf{r},\omega)$, we need to construct the Green's functions $G(\mathbf{x},\mathbf{s},\omega)$ and $G(\mathbf{x},\mathbf{r},\omega)$, and we will use ART for heterogeneous media. In this way, the Green's function is represented by a high-frequency approximation and its ART representation is given by

$$G(\mathbf{x},\mathbf{s},\omega) = A(\mathbf{x},\mathbf{s})\exp(i\omega t(\mathbf{x},\mathbf{s})), \quad (14)$$

where $A(\mathbf{x},\mathbf{s})$ is an amplitude term and $t(\mathbf{x},\mathbf{s})$ is the ray traveltime from the source position $\mathbf{s}$ to the image point $\mathbf{x}$.

Using the Green's functions with the ART approximation and making the assumption that the amplitude is a slowly varying function of space (Hildebrand and Carroll, 1993), equation 13 can be rewritten as

$$P(\mathbf{x},\omega) = -\,\omega^2 \int \partial_n t(\mathbf{x},\mathbf{s})A(\mathbf{x},\mathbf{s})d\mathbf{s} \int \partial_n t(\mathbf{x},\mathbf{r})A(\mathbf{x},\mathbf{r}) \times \exp(i\omega[t(\mathbf{x},\mathbf{s}) + t(\mathbf{x},\mathbf{r})])P(\mathbf{s},\mathbf{r},\omega)d\mathbf{r} \quad (15)$$

or

$$P(\mathbf{x},\omega) = -\,\omega^2 \int d\mathbf{s} \int W(\mathbf{x},\mathbf{s},\mathbf{r}) \times \exp(i\omega[t(\mathbf{x},\mathbf{s}) + t(\mathbf{x},\mathbf{r})])P(\mathbf{s},\mathbf{r},\omega)d\mathbf{r}, \quad (16)$$

where $t(\mathbf{x},\mathbf{s})$ and $t(\mathbf{x},\mathbf{r})$ are the traveltimes from the source and receiver locations, respectively, to the subsurface point $\mathbf{x}$, $\exp(i\omega[t(\mathbf{x},\mathbf{s}) + t(\mathbf{x},\mathbf{r})])$ corresponds to the time-delay operator, and the function $W(\mathbf{x},\mathbf{s},\mathbf{r})$ is defined as

$$W(\mathbf{x},\mathbf{s},\mathbf{r}) = \partial_n t(\mathbf{x},\mathbf{s})A(\mathbf{x},\mathbf{s})\partial_n t(\mathbf{x},\mathbf{r})A(\mathbf{x},\mathbf{r}). \quad (17)$$

PLANE-WAVE DEPTH MIGRATION-RECEIVER PLANE WAVES

The decomposition of the receiver data $P(\mathbf{s},\mathbf{r},\omega)$ is accomplished according to equation 6. Substituting equation 6 into equation 16 and moving the ray-parameter integral outside, we get

$$P(\mathbf{x},\omega) = -\,\omega^4 \int d\mathbf{p_r} \int W(\mathbf{x},\mathbf{s},\mathbf{r})\exp(i\omega t(\mathbf{x},\mathbf{s})) \times P(\mathbf{s},\mathbf{p_r},\omega)d\mathbf{s} \int \exp(i\omega[t(\mathbf{x},\mathbf{r}) - \mathbf{p_r}\cdot\mathbf{r}])d\mathbf{r}. \quad (18)$$

Here, we define the receiver vertical delay time, $\tau(\mathbf{x},\mathbf{r},\mathbf{p_r})$, as the receiver-traveltime contribution $t(\mathbf{x},\mathbf{r})$, minus the horizontal delay time from the receiver to the image position at the surface, $\mathbf{p_r}\cdot\mathbf{r}$:

$$\tau(\mathbf{x},\mathbf{r},\mathbf{p_r}) = t(\mathbf{x},\mathbf{r}) - \mathbf{p_r}\cdot\mathbf{r}. \quad (19)$$

Then, we let

$$P(\mathbf{x},\mathbf{p_r},\omega) = -\,\omega^4 \iint W(\mathbf{x},\mathbf{s},\mathbf{r})\exp(i\omega t(\mathbf{x},\mathbf{s})) \times P(\mathbf{s},\mathbf{p_r},\omega)\exp(i\omega\tau(\mathbf{x},\mathbf{r},\mathbf{p_r}))d\mathbf{s}d\mathbf{r} \quad (20)$$

be the migrated receiver plane-wave section for $\mathbf{p_r}$. The quantity $t(\mathbf{x},\mathbf{s})$ is the source traveltime, which must be calculated for each point-source position $\mathbf{s}$, and the quantity $\tau(\mathbf{x},\mathbf{r},\mathbf{p_r})$ is the receiver vertical delay time for each receiver and plane wave $\mathbf{p_r}$.

We notice that for $\mathbf{x} = (x,y,z)$, $\boldsymbol{\xi} = (x,y,0)$, arbitrary surface position $\boldsymbol{\eta}$, and ray parameter $\mathbf{p}$, we have (Figure 1)

$$\tau(\mathbf{x},\boldsymbol{\eta},\mathbf{p}) = \tau(\mathbf{x},\mathbf{p}) - \mathbf{p}\cdot\boldsymbol{\xi}, \quad (21)$$

where $\tau(\mathbf{x},\mathbf{p})$ is the vertical delay time for the plane wave with $\mathbf{p}$ computed from the origin to the isochron of $\mathbf{x}$. Looking at the two rays of Figure 1 and following the isochrons at the origin and the end of the ray for $\tau(\mathbf{x},\boldsymbol{\eta},\mathbf{p})$, we can see that the difference between $\tau(\mathbf{x},\boldsymbol{\eta},\mathbf{p})$ and $\tau(\mathbf{x},\mathbf{p})$ is the additional vertical delay time τ_ξ, which we see is equal to $\mathbf{p}\cdot\boldsymbol{\xi}$ by following its isochron back to the image-point projection. Thus,

$$\tau(\mathbf{x},\mathbf{r},\mathbf{p}_\mathbf{r}) = \tau(\mathbf{x},\mathbf{p}_\mathbf{r}) - \mathbf{p}_\mathbf{r}\cdot\boldsymbol{\xi}. \tag{22}$$

To develop a complete picture of the subsurface, we sum over all frequencies, stack all migrated plane-wave sections, and use equation 22 [since it is assumed that the amplitude is a slowly varying function of space, we may write $W(\mathbf{x},\mathbf{s},\mathbf{r}) = W(\mathbf{x},\mathbf{r})$]:

$$P(\mathbf{x}) = M(\mathbf{x})\int\!\!\int \omega^4 P(\mathbf{s},\mathbf{p}_\mathbf{r},\omega)d\omega d\mathbf{p}_\mathbf{r} \times \int \exp(i\omega(t(\mathbf{x},\mathbf{s}) + \tau(\mathbf{x},\mathbf{p}_\mathbf{r}) - \mathbf{p}_\mathbf{r}\cdot\boldsymbol{\xi})d\mathbf{s}, \tag{23}$$

where $M(\mathbf{x}) = -\int W(\mathbf{x},\mathbf{r})d\mathbf{r}$.

The filter ω^4 can be ignored here because it can be absorbed into recording and processing filtering effects (Claerbout, 1985). Noting that

$$\int P(\mathbf{s},\mathbf{p}_\mathbf{r},\omega)\exp(i\omega(t(\mathbf{x},\mathbf{s}) + \tau(\mathbf{x},\mathbf{p}_\mathbf{r}) - \mathbf{p}_\mathbf{r}\cdot\boldsymbol{\xi})d\omega = P(\mathbf{s},\mathbf{p}_\mathbf{r},t(\mathbf{x},\mathbf{s}) + \tau(\mathbf{x},\mathbf{p}_\mathbf{r}) - \mathbf{p}_\mathbf{r}\cdot\boldsymbol{\xi})), \tag{24}$$

we get

$$P(\mathbf{x}) = M(\mathbf{x})\int\!\!\int P(\mathbf{s},\mathbf{p}_\mathbf{r},t(\mathbf{x},\mathbf{s}) + \tau(\mathbf{x},\mathbf{p}_\mathbf{r}) - \mathbf{p}_\mathbf{r}\cdot\boldsymbol{\xi}))\times d\mathbf{p}_\mathbf{r}d\mathbf{s}. \tag{25}$$

PLANE-WAVE DEPTH MIGRATION-SOURCE PLANE WAVES

We now turn to the source plane-wave continuation operator. Substituting equation 8 into equation 16 and rearranging, we have

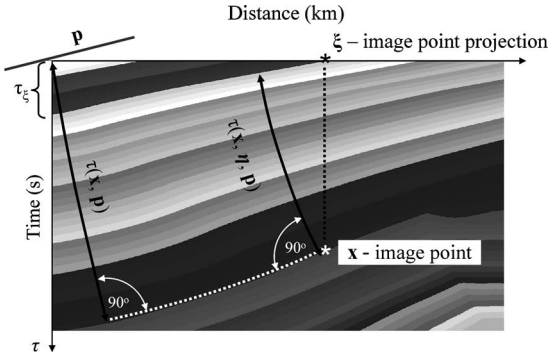

Figure 1. Isochrons (shown in shades of gray) for plane-wave vertical delay time. For the plane wave whose origin is in the upper left-hand corner of the velocity model, we can obtain the plane-wave vertical delay time at any image point $\mathbf{x}$ by following the isochrons through $\mathbf{x}$ and its projection onto the surface, point $\boldsymbol{\xi}$ to get $\tau(\mathbf{x},\boldsymbol{\eta},\mathbf{p}) = \tau(\mathbf{x},\mathbf{p}) - \mathbf{p}\cdot\boldsymbol{\xi}$, where $\mathbf{p}\cdot\boldsymbol{\xi} = \tau_\xi$.

$$P(\mathbf{x},\omega) = -\omega^4\int d\mathbf{p}_\mathbf{s}\int W(\mathbf{x},\mathbf{s},\mathbf{r})\exp(i\omega t(\mathbf{x},\mathbf{r})) \times P(\mathbf{p}_\mathbf{s},\mathbf{r},\omega)d\mathbf{r}\int \exp(i\omega[t(\mathbf{x},\mathbf{s}) - \mathbf{p}_\mathbf{s}\cdot\mathbf{s}]d\mathbf{s}. \tag{26}$$

Following the above developments, the source traveltime $t(\mathbf{x},\mathbf{s})$ can be combined with the source horizontal delay time to define the source vertical delay time as

$$\tau(\mathbf{x},\mathbf{s},\mathbf{p}_\mathbf{s}) = t(\mathbf{x},\mathbf{s}) - \mathbf{p}_\mathbf{s}\cdot\mathbf{s}. \tag{27}$$

Again, referring to Figure 1 and equation 21 for the source plane waves, we can write

$$\tau(\mathbf{x},\mathbf{s},\mathbf{p}_\mathbf{s}) = \tau(\mathbf{x},\mathbf{p}_\mathbf{s}) - \mathbf{p}_\mathbf{s}\cdot\boldsymbol{\xi}. \tag{28}$$

Equation 26 can be rewritten as

$$P(\mathbf{x},\mathbf{p}_\mathbf{s},\omega) = \omega^4 K(\mathbf{x})\int \exp(i\omega t(\mathbf{x},\mathbf{r})) \times P(\mathbf{p}_\mathbf{s},\mathbf{r},\omega)\exp(i\omega(\tau(\mathbf{x},\mathbf{p}_\mathbf{s}) - \mathbf{p}_\mathbf{s}\cdot\boldsymbol{\xi}))d\mathbf{r}, \tag{29}$$

where $K(\mathbf{x}) = -\int W(\mathbf{x},\mathbf{s})d\mathbf{s}$.

Now, the quantity $t(\mathbf{x},\mathbf{r})$, which is the receiver traveltime, can be calculated by simulating a point source at the receiver locations. Equations 18 or 26 and equations 20 or 29 are identical except for the plane waves being considered and are the integrals required for the wavefield continuation for either source or receiver plane waves. Each migrated plane-wave section results from the superposition of all source or receiver contributions, like the areal source method (Romero et al., 2000) or the delayed-shot migration method (Liu et al., 2002; Zhang et al., 2003). We again need to sum over all frequencies and stack all the migrated plane-wave sections to develop the complete picture of the subsurface:

$$P(\mathbf{x}) = K(\mathbf{x})\int\!\!\int P(\mathbf{p}_\mathbf{s},\mathbf{r},t(\mathbf{x},\mathbf{r}) + \tau(\mathbf{x},\mathbf{p}_\mathbf{s}) - \mathbf{p}_\mathbf{s}\cdot\boldsymbol{\xi})d\mathbf{p}_\mathbf{s}d\mathbf{r}. \tag{30}$$

PLANE-WAVE DEPTH MIGRATION — SOURCE AND RECEIVER PLANE WAVES

We can also represent the source-receiver data $P(\mathbf{s},\mathbf{r},\omega)$ as an inverse slant-stack transform for both the source and the receiver plane waves, $\mathbf{p}_\mathbf{s}$ and $\mathbf{p}_\mathbf{r}$. Substituting equation 10 into equation 16 and moving both ray-parameter integrals outside, we get

$$P(\mathbf{x},\omega) = -\omega^6\int\!\!\int W(\mathbf{x},\mathbf{s},\mathbf{r})P(\mathbf{p}_\mathbf{s},\mathbf{p}_\mathbf{r},\omega)d\mathbf{p}_\mathbf{s}d\mathbf{p}_\mathbf{r} \times \int\!\!\int \exp(i\omega[t(\mathbf{x},\mathbf{s}) + t(\mathbf{x},\mathbf{r}) - \mathbf{p}_\mathbf{s}\cdot\mathbf{s} - \mathbf{p}_\mathbf{r}\cdot\mathbf{r}]) \times d\mathbf{s}d\mathbf{r}. \tag{31}$$

Using the definitions for $\tau(\mathbf{x},\mathbf{s},\mathbf{p}_\mathbf{s})$ and $\tau(\mathbf{x},\mathbf{r},\mathbf{p}_\mathbf{r})$, we have

$$P(\mathbf{x},\mathbf{p_s},\mathbf{p_r},\omega) = -\omega^6 P(\mathbf{p_s},\mathbf{p_r},\omega)\iint W(\mathbf{x},\mathbf{s},\mathbf{r}) \times \exp(i\omega(\tau(\mathbf{x},\mathbf{s},\mathbf{p_s}) + \tau(\mathbf{x},\mathbf{r},\mathbf{p_r})) \times d\mathbf{s}d\mathbf{r}. \quad (32)$$

Using equations 22 and 28 simultaneously, and after summing over all frequencies, $P(\mathbf{x},\mathbf{p_s},\mathbf{p_r})$ is the migrated section for the plane-wave pair $\mathbf{p_s}$, $\mathbf{p_r}$:

$$P(\mathbf{x},\mathbf{p_s},\mathbf{p_r}) = L(\mathbf{x})\int \omega^6 P(\mathbf{p_s},\mathbf{p_r},\omega) \times \exp(i\omega(\tau(\mathbf{x},\mathbf{p_s}) + \tau(\mathbf{x},\mathbf{p_r}) - (\mathbf{p_s}+\mathbf{p_r})\cdot\boldsymbol{\xi}) \times d\omega, \quad (33)$$

where $L(\mathbf{x}) = -\int\int W(\mathbf{x},\mathbf{s},\mathbf{r})d\mathbf{s}d\mathbf{r}$.

The final image is formed by summing over all plane-wave combinations:

$$P(\mathbf{x}) = L(\mathbf{x})\iiint \omega^6 P(\mathbf{p_s},\mathbf{p_r},\omega)\exp(i\omega(\tau(\mathbf{x},\mathbf{p_s}) + \tau(\mathbf{x},\mathbf{p_r}) - (\mathbf{p_s}+\mathbf{p_r})\cdot\boldsymbol{\xi})d\omega d\mathbf{p_s}d\mathbf{p_r}. \quad (34)$$

Using the same argument as the transition from equation 23 to equation 25, we arrive at the double plane-wave imaging formula,

$$P(\mathbf{x}) = L(\mathbf{x})\iint P(\mathbf{p_s},\mathbf{p_r},\tau(\mathbf{x},\mathbf{p_s}) + \tau(\mathbf{x},\mathbf{p_r}) - (\mathbf{p_s}+\mathbf{p_r})\cdot\boldsymbol{\xi})d\mathbf{p_s}d\mathbf{p_r}. \quad (35)$$

The difference between this approach and the usual Kirchhoff-migration integral rests primarily in the treatment of the source and receiver ray-traveltime computations. Similar expressions for coupled plane-wave Kirchhoff modeling are reported in Sen and Frazer (1991), and those for imaging are reported in Fokkema and van den Berg (1993) and Tatalovic et al. (1991). Here, the receiver ray, as well as the source ray, is traced back into depth, and both have a surface take-off angle determined by the ray parameter that matches the ray parameters of the double slant-stack-transformed wavefield. The wavefronts are assumed planar only at the surface, and the source and receiver vertical delay times must be calculated numerically using an eikonal solver, e.g., Schneider et al. (1992), or point-by-point ray tracing for each plane wave, e.g., Farra and Madariaga (1987). Then the image is obtained by sampling the plane-wave data for all source and receiver plane-wave combinations for each image point.

In the above derivations for source, receiver, and simultaneous source and receiver plane-wave imaging, we have neglected a detailed discussion of the amplitude terms to emphasize the kinematic aspects of the plane-wave migration methods. To implement a true-amplitude version of the method requires a more careful consideration of the amplitude term. This is presented in Appendix A, where we use Chapman-Maslov asymptotic theory (Chapman and Drummond, 1982; Chapman, 2004) to represent the Green's function in terms of plane waves and explicitly take into account the amplitude terms. Equations A-7, A-14, and A-15 are analogous to equations 35, 25, and 30, respectively.

PLANE-WAVE DEPTH MIGRATION — OFFSET PLANE WAVES

The above development can be translated to offset coordinates. If we make the change of variables

$$\mathbf{o} = \mathbf{r} - \mathbf{s}, \qquad \mathbf{s}' = \mathbf{s}, \quad (36)$$

then, using the chain rule, we get

$$\mathbf{p_r} = \frac{\partial t}{\partial \mathbf{r}} = \frac{\partial t}{\partial \mathbf{o}}\frac{\partial \mathbf{o}}{\partial \mathbf{r}} + \frac{\partial t}{\partial \mathbf{s}'}\frac{\partial \mathbf{s}'}{\partial \mathbf{r}} = \frac{\partial t}{\partial \mathbf{o}} = \mathbf{p_o},$$

$$\mathbf{p_s} = \frac{\partial t}{\partial \mathbf{s}} = \frac{\partial t}{\partial \mathbf{o}}\frac{\partial \mathbf{o}}{\partial \mathbf{s}} + \frac{\partial t}{\partial \mathbf{s}'}\frac{\partial \mathbf{s}'}{\partial \mathbf{s}} = -\frac{\partial t}{\partial \mathbf{o}} + \frac{\partial t}{\partial \mathbf{s}'} = \mathbf{p_{s'}} - \mathbf{p_o}, \quad (37)$$

where $\partial t/\partial \mathbf{r}$, $\partial t/\partial \mathbf{s}$, etc., are partial gradients and $\partial \mathbf{o}/\partial \mathbf{r}$, $\partial \mathbf{o}/\partial \mathbf{s}$, etc., are 3×3 gradient matrices (in particular, $\partial \mathbf{o}/\partial \mathbf{r}$ is a 3×3 unit matrix). Assuming wavefield invariance, i.e.,

$$P(\mathbf{s},\mathbf{r},t) = P'(\mathbf{s}',\mathbf{o},t),\ P(\mathbf{p_s},\mathbf{p_r},\tau) = P'(\mathbf{p_{s'}},\mathbf{p_o},\tau), \quad (38)$$

noting that the Jacobian is $d\mathbf{p_s}d\mathbf{p_r} = d\mathbf{p_{s'}}d\mathbf{p_o}$ and dropping the primes after the change of variables, equation 35 becomes

$$P(\mathbf{x}) = L(\mathbf{x})\iint P(\mathbf{p_s},\mathbf{p_o},\tau(\mathbf{x},\mathbf{p_s}-\mathbf{p_o}) + \tau(\mathbf{x},\mathbf{p_o}) - \mathbf{p_s}\cdot\boldsymbol{\xi}) \times d\mathbf{p_s}d\mathbf{p_o}. \quad (39)$$

Again, the final image is formed by sampling the $\mathbf{p_s}-\mathbf{p_o}$ data volume for all source and offset plane-wave combinations for each image point.

In a similar manner, we can transform equations 25 and 30 to source-offset coordinates to obtain equations (Akbar et al., 1996)

$$P(\mathbf{x}) = M(\mathbf{x})\iint P(\mathbf{s},\mathbf{p_o},t(\mathbf{x},\mathbf{s}) + \tau(\mathbf{x},\mathbf{p_o}) - \mathbf{p_o}\cdot\boldsymbol{\xi})) \times d\mathbf{p_o}d\mathbf{s} \quad (40)$$

and

$$P(\mathbf{x}) = K(\mathbf{x})\iint P(\mathbf{p_s},\mathbf{o},t(\mathbf{x},\mathbf{o}) + \tau(\mathbf{x},\mathbf{p_s}) - \mathbf{p_s}\cdot\boldsymbol{\xi})d\mathbf{p_s}d\mathbf{o}, \quad (41)$$

where $t(\mathbf{x},\mathbf{o})$ is the equivalent of $t(\mathbf{x},\mathbf{r})$ for the receiver $\mathbf{r}$ corresponding to the offset $\mathbf{o}$.

P_S-P_O PLANE-WAVE TRANSFORMATION

Figure 2 shows schematically how 2D shot gathers are transformed over source-receiver offset to generate the typical τ-$\mathbf{p_o}$ gathers. The data are then sorted into constant $\mathbf{p_o}$ sections. A constant

$\mathbf{p_o}$ section appears similar to a constant-offset section, except that the times of arrival are now vertical delay times instead of traveltimes and the data for each source position have a common angle of incidence at the surface instead of a common offset. These constant $\mathbf{p_o}$ data are then slant stacked over source positions $\mathbf{s}$ to generate the $P(\mathbf{p_s}, \mathbf{p_o}, \tau)$ data used for imaging in equation 39.

Consider a model consisting of five constant-velocity layers separated by four dipping interfaces. Seismic data for a constant $\mathbf{p_o}$ gather (Figure 3a) would look similar to a constant-offset gather. In Figure 3a, the four dipping events correspond to reflections, and their $\mathbf{p_s}$ transform is shown in Figure 3b. As expected, the events localize at the $\mathbf{p_s}$ corresponding to their vertical delay-time dips $d\tau/d\mathbf{s}$ in Figure 3a. The horizontal reflector now appears at $\mathbf{p_s} = 0.0$ s/km, and positive and negative dips are separated.

Now consider a model consisting of four diffractors in a constant-velocity medium. Seismic data for a constant $\mathbf{p_o}$ gather (Figure 3c) would look similar to a constant-offset gather. In Figure 3c, the four hyperbolas correspond to diffractions, and the dots indicate where the slope $d\tau/d\mathbf{s}$ or $\mathbf{p_s} = 0.0$ s/km. The $\mathbf{p_s}$ transform is shown in Figure 3d, and the intercept times for the $\mathbf{p_s} = 0.0$ s/km events are again shown as dots.

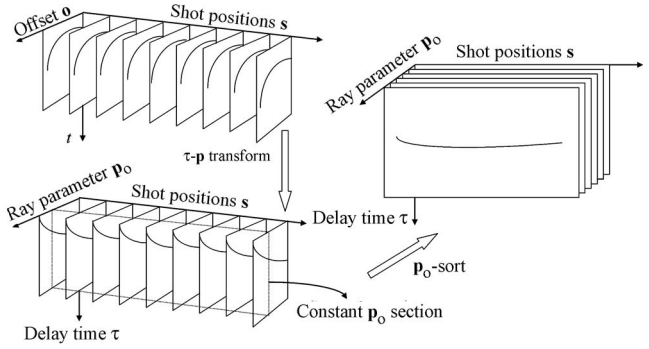

Figure 2. Seismic data recorded as a function of source position $\mathbf{s}$ and offset $\mathbf{o}$ are transformed into offset plane waves $\mathbf{p_o}$ and vertical delay time τ. Data for each constant-offset plane wave $\mathbf{p_o}$ are gathered into a section for the second slant stack.

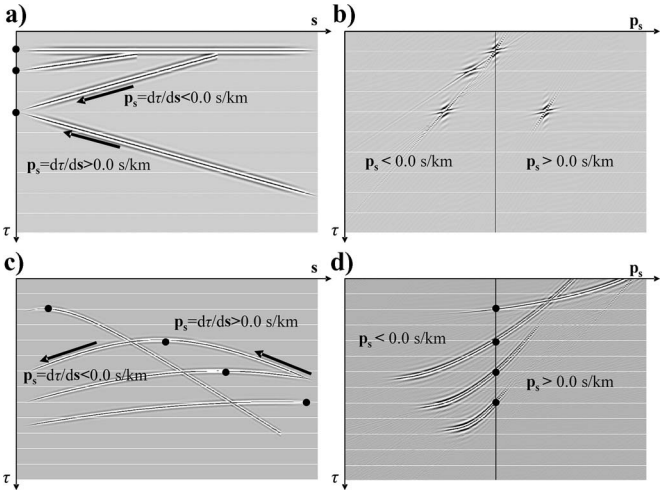

Figure 3. (a) Data for a constant-offset ray-parameter section $\mathbf{p_o}$ are summed along linear τ-$\mathbf{s}$ trajectories to form the τ-$\mathbf{p_s}$-$\mathbf{p_o}$ data. (b) The four constant time dips of the offset plane-wave section in (a) map to four points in the $\mathbf{p_s}$ domain. (c) Diffractions recorded on a constant-offset ray-parameter section $\mathbf{p_o}$ are also summed along linear τ-$\mathbf{s}$ trajectories to form the τ-$\mathbf{p_s}$-$\mathbf{p_o}$ data; (d) The four diffractions recorded in (a) to four events in the $\mathbf{p_s}$ domain. The dots indicate $\mathbf{p_s} = 0.0$ s/km.

POINT SOURCE-RECEIVER AND PLANE-WAVE IMAGING

The synthetic examples are based on a 2D staggered-grid elastic finite-difference simulation (Levander, 1988) of the SEG/EAGE 3D salt model (Aminzadeh et al., 1997). The velocity function used is a 2D slice from this model (Figure 4). The finite-difference data were acquired every 0.02 km along the top of the model for 675 shot positions. The acquisition proceeded from the left ($X = 0.0$ km) to the right ($X = 13.48$ km). We simulated a marine survey with a receiver towed behind the ship. There were 240 channels acquired with the first complete shot gather occurring at shot point 240 ($X = 4.78$ km). The receiver spacing was 0.02 km. The first layer was water, and only pressure was recorded. Absorbing boundaries were added to the model to limit reflections from the edges and bottom of the model and to minimize surface-related multiples. Four example shot records from the middle of the survey and over the salt are shown in Figure 5.

The original shot gathers were transformed into the offset plane-wave domain by simple slant stacking using equation 3. There were 121 plane-wave seismograms for ray parameters +0.6 to −0.6 s/km every 0.01 s/km recovered from the input shot gathers (Figure 6). The theoretical sampling required is $1/(f_{\max} x_{\max})$ or, for 30 Hz, 0.007 s/km. The migrated and stacked plane-wave data using equation 40 are shown in Figure 7.

The original shot data were then gathered into common-receiver gathers (Figure 8). We note that now the first receiver has full coverage from the 240 shots that it recorded. But, on the right-hand side, because the shooting stopped at the end of the model, the number of traces continuously decreases from $X = 8.68$ km to the end of the line. The data were transformed to the plane-wave domain using equation 3 once more (with the roles of sources and receivers interchanged). Again, 121 plane-wave seismograms for ray parameters +0.6 to −0.6 s/km every 0.01 s/km were recovered from the input common-receiver gathers. Figure 9 shows the transformed data.

Comparing Figures 5 and 8 and Figures 6 and 9, we note that different events are stronger in each gather and that their moveouts are different. The plane-wave gathers in Figures 6 and 9 show that each

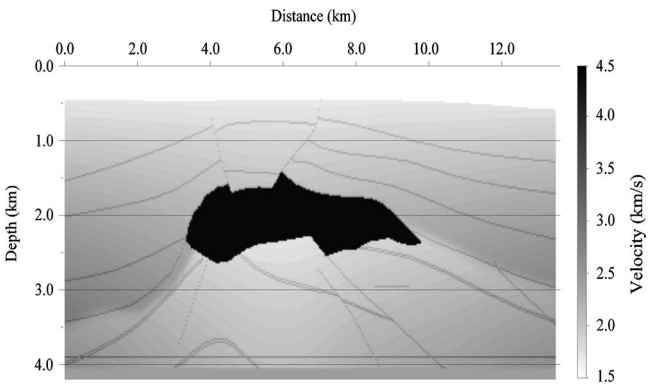

Figure 4. 2D slice from SEG/EAGE 3D salt model used in this study.

gather has recorded plane waves from predominantly opposite directions. This is as we expect from the acquisition geometry and gathering process. The plane-wave-migrated result for the common-receiver gathers using equation 41 is shown in Figure 10.

For the point source or receiver, we used an eikonal solver (Schneider et al., 1992) to calculate the traveltimes. For the plane-wave traveltimes, we used a point-by-point, grid-based ray-tracing algorithm (Farra and Madariaga, 1987). In both cases, a constant-offset ray-parameter plane-wave section was collected from the plane-wave gathers and migrated independently of the others. Once all plane-wave sections were migrated, the resulting common-image gathers were stacked to generate the final images, i.e., Figures 7 and 10. In both examples, 121 plane-wave vertical delay time tables and 675 point-source traveltime tables were computed.

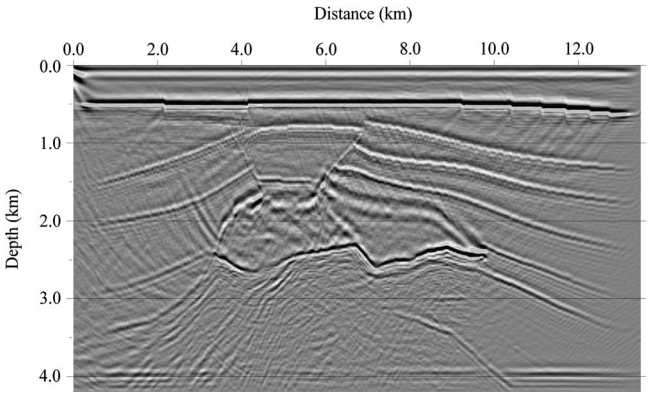

Figure 7. Migrated common-shot receiver plane-wave gathers. A total of 121 receiver plane-wave sections were migrated and stacked to produce the image.

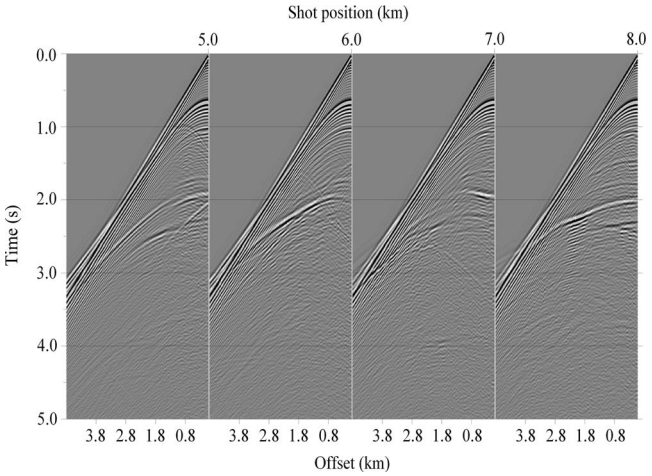

Figure 5. Finite-difference common-shot gathers at source positions 5, 6, 7, and 8 km, simulating a marine survey with the array towed behind the ship. A total of 240 channels were acquired with a receiver spacing of 0.02 km. The maximum offset is 4.78 km.

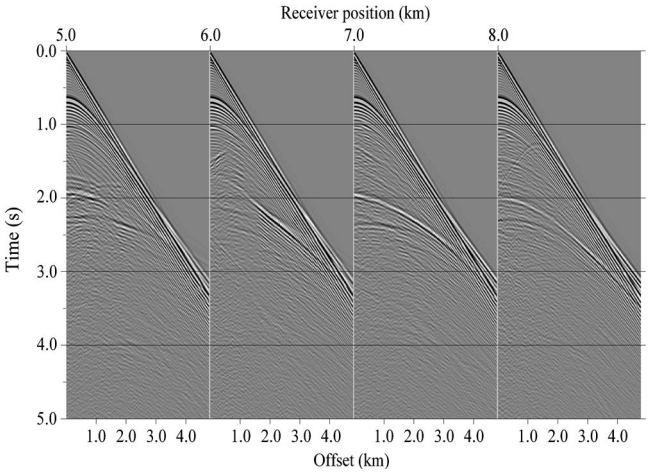

Figure 8. Finite-difference common-receiver gathers at receiver positions 5, 6, 7, and 8 km collected from the original common-shot gathers. The maximum offset is 4.78 km.

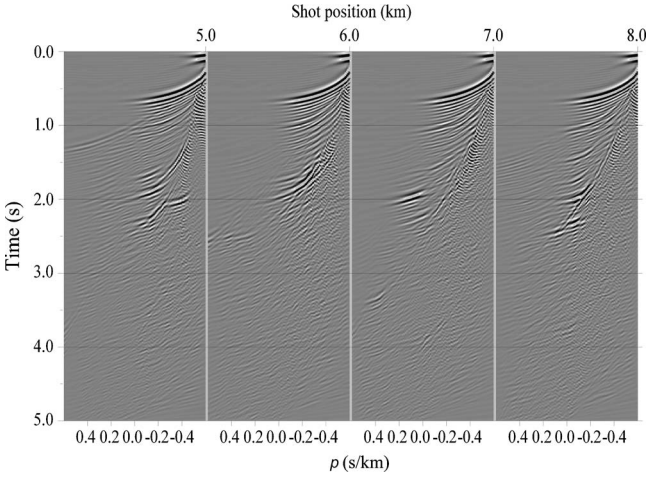

Figure 6. The τ-p transformed shot-point gathers at source positions 5, 6, 7, and 8 km, corresponding to common-shot gathers of Figure 5; 121 traces in each panel correspond to ray parameters from +0.6 to −0.6 s/km every 0.01 s/km.

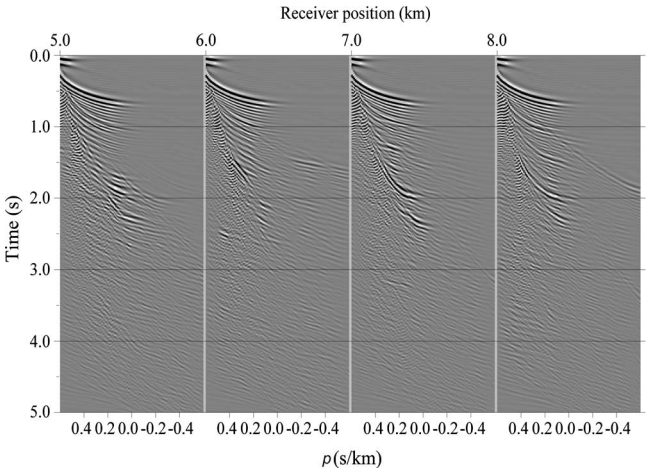

Figure 9. The τ-p transformed receiver gathers at receiver positions 5, 6, 7, and 8 km, corresponding to the receiver gathers of Figure 8; 121 traces in each panel correspond to ray parameters from +0.6 to −0.6 s/km every 0.01 s/km.

In Figure 7, the image from the plane-wave-transformed shot gathers, the left side of the deep structure is not recovered as well as in Figure 10 because of the acquisition geometry. The same is true for the right side of the section for the migrated plane-wave common-receiver gathers in Figure 10. The final result is formed by stacking the two images (Figure 11). In this way, we explicitly included source-receiver reciprocity by physically generating and then imaging the receiver gathers.

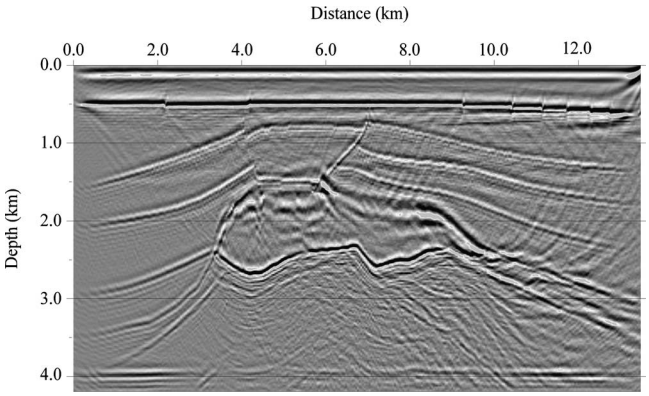

Figure 10. Migrated common-receiver source plane-wave gathers; 121 source plane-wave sections were migrated and stacked to produce the image.

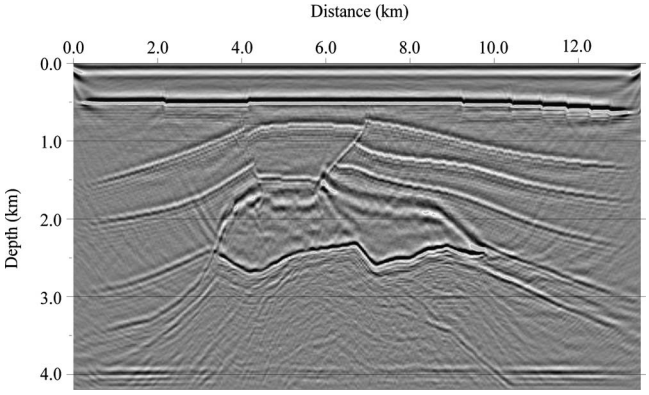

Figure 11. Combined migrated shot and receiver gathers (i.e., reciprocity included).

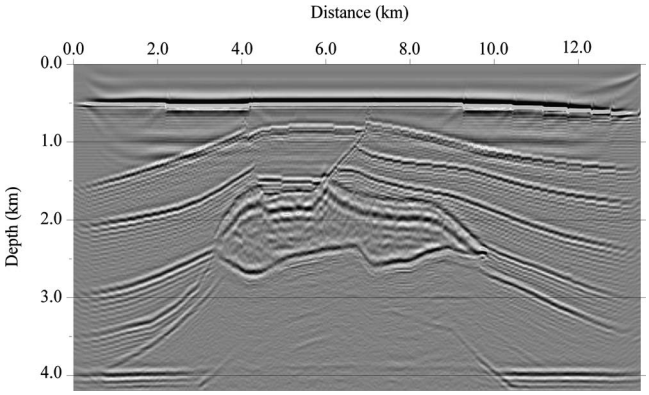

Figure 12. Conventional *x-t* Kirchhoff-migration result for the same data, plotted with the same display parameters as in Figure 11.

Figure 12 is an example of *x-t* Kirchhoff imaging for the same input data using seismic Unix (SU). Comparing Figures 11 and 12, we see that the overall image quality is similar. The plane-wave result has more artifacts but images the subsalt arrivals on the right side better. Also, the deepest subsalt event is more continuous. The *x-t* implementation requires, in theory, 241 traveltime calculations per shot for 675 shots (total of 162, 675), assuming unique source and receiver positions. The plane-wave result required 675 plus 121 (total of 796) traveltime calculations.

DOUBLE PLANE-WAVE IMAGING

The original simulated marine (one-sided) data can be transformed to construct both source and receiver plane waves simultaneously using equations 9 or 11. This process completely transforms the data into source and receiver or source and offset plane-wave components. We again used a ray-parameter sampling of 0.01 s/km for the $\mathbf{p_s}$-$\mathbf{p_o}$ volume. For the $\mathbf{p_s}$ sampling, the theoretical rate is $1/(\omega_{max} x_{max})$, which is 0.002 s/km. We will show several sections through the $\mathbf{p_s}$-$\mathbf{p_o}$ volume generated using equation 11.

Figure 13 shows the case for all $\mathbf{p_o}$ plane waves when $\mathbf{p_s}$ = 0.2, 0.0, and −0.2 s/km from left to right in three panels. Here, the $\mathbf{p_s}$ = 0.0 s/km (center) gather corresponding to horizontal reflectors dominates the others and appears similar to the τ-$\mathbf{p_o}$ transform of a single shot gather. Figure 14 shows the opposite case, for the same values and all source plane waves from left to right in three panels. The middle and right panels have more energy because we used the original shot gathers' τ-$\mathbf{p}$ transforms (Figure 6). Had we used the receiver gathers, most of the energy would appear in the middle and left panels (Figure 9).

The $\mathbf{p_s}$-$\mathbf{p_o}$ volume was migrated using equation 39 and the point-by-point ray-tracing algorithm to calculate the vertical delay times. Each constant-offset ray-parameter plane-wave section was migrated independently of the others and in parallel. Once all plane-wave sections were migrated, the resulting common-image gathers were stacked to generate the final image. Plane-wave vertical delay times were reused once computed as appropriate. For example, vertical delay times for any $\mathbf{p}$, whether $\mathbf{p_r}$, $\mathbf{p_o}$, or $\mathbf{p_s}$, can be used, whether we need a $\mathbf{p_s}$, $\mathbf{p_r}$, or a $\mathbf{p_o}$, as long as it has previously been computed.

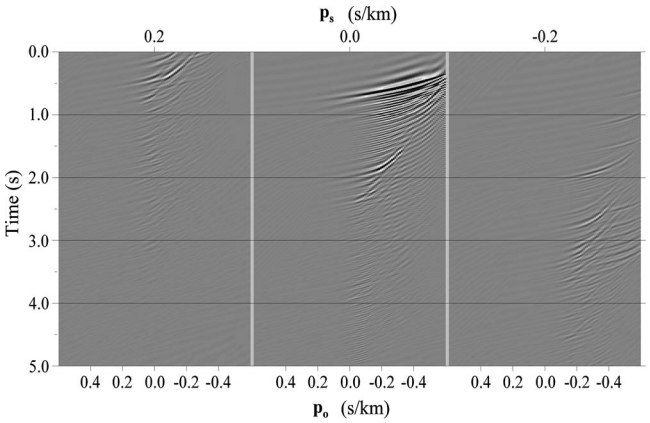

Figure 13. $\mathbf{p_s}$ cross sections from $\mathbf{p_s}$-$\mathbf{p_o}$ volume.

Figure 15 shows the result for a targeted imaging where we used all 121 $\mathbf{p}_o$ plane waves but limit the $\mathbf{p}_s$ aperture to −0.1 to +0.1 s/km about each $\mathbf{p}_o$ plane wave being imaged. This means we are imaging principally reflection data. Figure 15 has a low spatial-frequency appearance because only reflections were imaged using a very limited $\mathbf{p}_s$ aperture. This approach is useful for velocity analysis because the imaging is computationally very fast, and we can add more $\mathbf{p}_s$ aperture as the velocity model becomes better determined. In Figure 16, the $\mathbf{p}_s$ aperture increases to −0.6 to +0.6 s/km (a total of 121 plane-wave delay times computed), and the results show improved spatial resolution as more diffracted energy is included in the final image. For this result, we did not include source-receiver reciprocity, but it still compares favorably to Figure 11. The weak image of the base of the salt on the left-hand side in Figure 16 is only imaged when the receiver gathers are used, i.e., in the source plane-wave example in Figure 10.

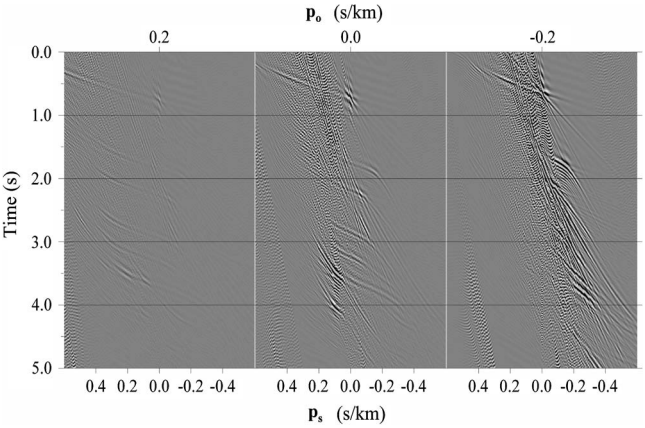

Figure 14. The $\mathbf{p}_o$ cross sections from $\mathbf{p}_s$-$\mathbf{p}_o$ volume.

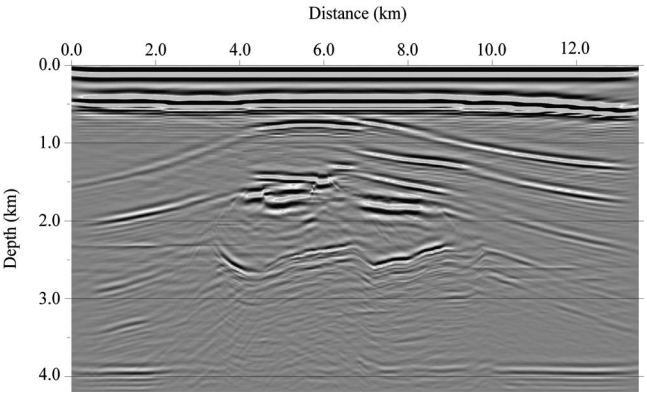

Figure 15. The $\mathbf{p}_s$-$\mathbf{p}_o$ migrated image: $\mathbf{p}_s$ values range from −0.1 to 0.1 s/km; $\mathbf{p}_o$ values range from −0.6 to 0.6 s/km.

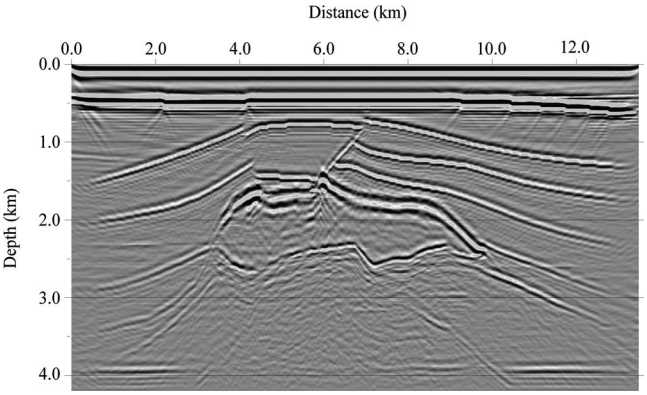

Figure 16. The $\mathbf{p}_s$-$\mathbf{p}_o$ migrated image: $\mathbf{p}_s$ values range from −0.6 to 0.6 s/km; $\mathbf{p}_o$ values range from −0.6 to 0.6 s/km.

REAL DATA EXAMPLE

Figure 17 shows a prestack depth-migrated image for a marine line acquired offshore Nicaragua. The box indicates the data of Figure 18, which shows the details of **s**-$\mathbf{p}_o$ common-image gathers after $\mathbf{p}_s$-$\mathbf{p}_o$ imaging. The high-resolution input data consisted of 901 shots spaced every 0.0125 km with 168 traces per shot, also spaced at 0.0125 km. The record length was 4096 samples, and the sampling interval was 0.001 s. The farthest offset was 2.1 km, and the nearest offset was 0.0125 km.

The shot gathers were transformed to $\mathbf{p}_s$-$\mathbf{p}_o$ gathers and imaged using equation 39. Fifty equally spaced $\mathbf{p}_o$ ray parameters from 0.1 to −0.4 s/km were used, and 242 equally spaced $\mathbf{p}_s$ ray parameters from 0.6 to −0.6 s/km were used. There were 151,368 input-data traces, but only 6050 traces were used in the imaging. Further, only 242 unique delay-time tables were needed.

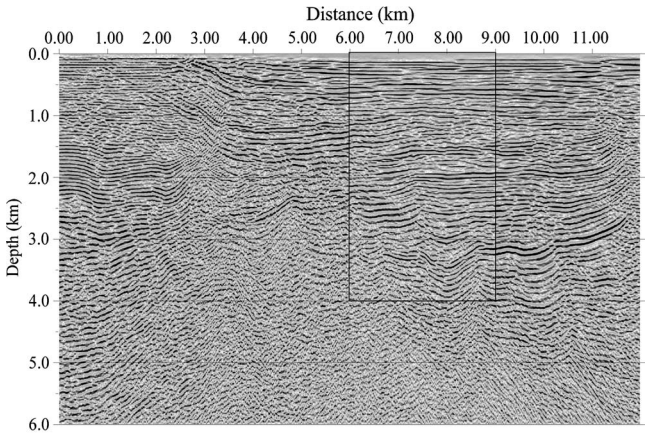

Figure 17. Prestack $\mathbf{p}_s$-$\mathbf{p}_o$ depth-migrated image for line 44 of the Nicaragua data.

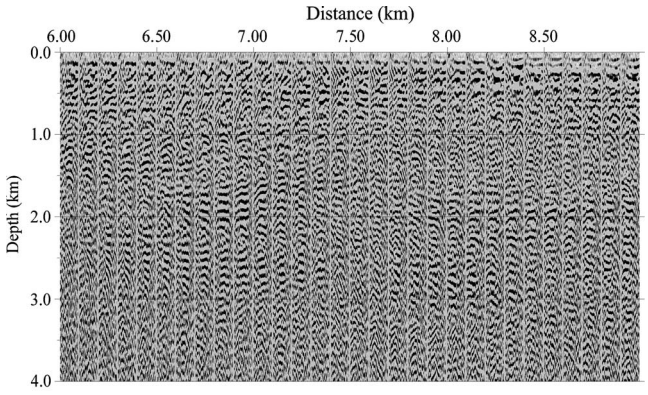

Figure 18. Common-image gathers for line 44 of the Nicaragua data after $\mathbf{p}_s$-$\mathbf{p}_o$ imaging.

Migration velocities were determined using very fast simulated annealing (VFSA), as described by Sen and Stoffa (1991), Akbar (1997), and Varela et al. (1998). The resulting common-image gathers in Figure 18 are reasonably well imaged for the shallow part of the section. The $\mathbf{s}$-$\mathbf{p}_o$ depth-migration residuals for the deeper events could now be used to refine the velocity model using the method of Jiao et al. (2002).

CONCLUSIONS

Modern seismic data can be transformed into source, receiver, or offset plane-wave components, and these compact data volumes can be imaged to depth with minimal (i.e., source- and receiver-position independent) traveltime computations. Plane-wave migration has several advantages over conventional offset-domain migration methods. First, the plane-wave transforms regularize the observational data as part of a preimaging process. Second, plane-wave data may be sparser than the recorded data, so smaller data volumes are used in the imaging algorithm (see examples above). In addition, relevant subsets of plane-wave components can be used for target-illumination and velocity-analysis studies. The main advantage, however, is that the vertical delay times that need to be computed are independent of the source and receiver positions except for a simple horizontal delay-time correction. Consequently, many of the same vertical delay times are required for imaging either source, receiver, or offset plane waves and need be calculated only once. Staging over plane-wave aperture is suggested as a useful tool for velocity analysis, as we can concentrate on reflected arrivals and form trial images rapidly. High spatial-resolution imaging can be performed by simply adding more source plane-wave components as the velocity model becomes better known, which should be particularly advantageous for 3D applications. Finally, the methods described here can be implemented for anisotropy by changing the vertical delay-time algorithm and using the appropriate amplitude corrections. This is because the plane-wave domain is the equivalent of a phase-velocity representation, where anisotropy can be taken into account exactly.

ACKNOWLEDGMENTS

The authors would like to thank Svein Vaage for his insight and encouragement. We acknowledge the support of NSF ODP grant OCE-0241179 for providing the data used in this paper. We also thank associate editor I. Lecomte and A. Weglein for their thorough reviews, comments, and suggestions that improved this manuscript.

APPENDIX A

PLANE-WAVE IMAGING USING MASLOV GREEN'S FUNCTION

Source and receiver plane waves

In a homogeneous medium, we can express the Green's function in terms of plane waves and derive a Kirchhoff integral in the plane-wave domain (Sen and Frazer, 1991). For inhomogeneous media, we make use of Chapman-Maslov asymptotic theory (Chapman and Drummond, 1982; Chapman, 2004), in which the Green's function is given by

$$G(\mathbf{x},\mathbf{s},\omega) = \omega^2 \int A_s(\mathbf{x},\mathbf{p_s}) \exp(i\omega t(\mathbf{x},\mathbf{p_s}))\, d\mathbf{p_s}, \tag{A-1}$$

where the integration is carried over rays characterized by a parameter $\mathbf{p}$. In our application, $\mathbf{p}$ is the horizontal slowness at the surface.

The amplitude term is given by

$$A_s(\mathbf{x},\mathbf{p_s}) = \left|\frac{dp_{11}}{d\mathbf{p_s}}\right|^{1/2} \left|\frac{dx_{11}}{d\mathbf{p_s}}\right|^{1/2} \times \exp\left(i\frac{\pi}{4}\left(\mathrm{sgn}\left(\frac{dp_{11}}{d\mathbf{p_s}}\frac{dx_{11}}{d\mathbf{p_s}}\right) - 1\right)\right), \tag{A-2}$$

where $\hat{p}_{11}\cdot\hat{n} = 0, \hat{x}_{11}\cdot\hat{n} = 0$. The phase term is given by

$$t(\mathbf{x},\mathbf{p_s}) = \tau(\mathbf{x},\mathbf{p_s}) + \mathbf{p_s}\cdot(\mathbf{s} - \boldsymbol{\xi}) \tag{A-3}$$

(see Figure 1). Similar expressions can be written for $G(\mathbf{x},\mathbf{r},\omega)$ (see below).

Thus, using equations A-1 and A-3, from equation 13, we have

$$\begin{aligned} P(\mathbf{x},\omega) = -\,\omega^6 \iint & A_s(\mathbf{x},\mathbf{p_s})\partial_n t(\mathbf{x},\mathbf{p_s}) \\ & \times A_r(\mathbf{x},\mathbf{p_r})\partial_n t(\mathbf{x},\mathbf{p_r})\, d\mathbf{p_s} d\mathbf{p_r} \\ & \times \exp(i\omega(\tau(\mathbf{x},\mathbf{p_s}) + \tau(\mathbf{x},\mathbf{p_r}) - (\mathbf{p_s}+\mathbf{p_r})\cdot\boldsymbol{\xi})) \\ & \times \iint P(\mathbf{s},\mathbf{r},\omega)\exp(i\omega(\mathbf{p_s}\cdot\mathbf{s} + \mathbf{p_r}\cdot\mathbf{r}))\, d\mathbf{s} d\mathbf{r}. \end{aligned} \tag{A-4}$$

From equation 9, it follows that

$$\begin{aligned} P(\mathbf{x},\omega) = -\,\omega^6 \iint & A_s(\mathbf{x},\mathbf{p_s})\partial_n t(\mathbf{x},\mathbf{p_s}) A_r(\mathbf{x},\mathbf{p_r})\partial_n t(\mathbf{x},\mathbf{p_r}) \\ & \times \exp(i\omega(\tau(\mathbf{x},\mathbf{p_s}) + \tau(\mathbf{x},\mathbf{p_r}) - (\mathbf{p_s}+\mathbf{p_r})\cdot\boldsymbol{\xi})) \\ & \times P(\mathbf{p_s},\mathbf{p_r},\omega)\, d\mathbf{p_s} d\mathbf{p_r}. \end{aligned} \tag{A-5}$$

Ignoring filter ω^6, after summing over all frequencies, we get

$$\begin{aligned} P(\mathbf{x}) = -\iint & A_s(\mathbf{x},\mathbf{p_s}) A_r(\mathbf{x},\mathbf{p_r})\partial_n t(\mathbf{x},\mathbf{p_s})\partial_n t(\mathbf{x},\mathbf{p_r}) \\ & \times P(\mathbf{p_s},\mathbf{p_r},\tau(\mathbf{x},\mathbf{p_s}) + \tau(\mathbf{x},\mathbf{p_r}) - (\mathbf{p_s}+\mathbf{p_r})\cdot\boldsymbol{\xi}) \\ & \times d\mathbf{p_s} d\mathbf{p_r}. \end{aligned} \tag{A-6}$$

If we now define

$$L(\mathbf{x},\mathbf{p_s},\mathbf{p_r}) = -\,A_s(\mathbf{x},\mathbf{p_s}) A_r(\mathbf{x},\mathbf{p_r})\partial_n t(\mathbf{x},\mathbf{p_s})\partial_n t(\mathbf{x},\mathbf{p_r}),$$

then equation A-6 becomes the double plane-wave imaging formula:

$$\begin{aligned} P(\mathbf{x}) = \iint & L(\mathbf{x},\mathbf{p_s},\mathbf{p_r}) P(\mathbf{p_s},\mathbf{p_r},\tau(\mathbf{x},\mathbf{p_s}) \\ & + \tau(\mathbf{x},\mathbf{p_r}) - (\mathbf{p_s}+\mathbf{p_r})\cdot\boldsymbol{\xi})\, d\mathbf{p_s} d\mathbf{p_r}. \end{aligned} \tag{A-7}$$

Receiver plane waves

Here, we follow an alternative development in which we use ART for the source-related Green's function, while employing Chapman–Maslov formula for the receiver Green's function, i.e.,

$$G(\mathbf{x},\mathbf{r},\omega) = \omega^2 \int A_r(\mathbf{x},\mathbf{p_r})\exp(i\omega t(\mathbf{x},\mathbf{p_r}))d\mathbf{p_r}, \quad \text{(A-8)}$$

where

$$A_r(\mathbf{x},\mathbf{p_r}) = \left|\frac{dp_{11}}{d\mathbf{p_r}}\right|^{1/2}\left|\frac{dx_{11}}{d\mathbf{p_r}}\right|^{1/2} \times \exp\left(i\frac{\pi}{4}\left(\mathrm{sgn}\left(\frac{dp_{11}}{d\mathbf{p_r}}\frac{dx_{11}}{d\mathbf{p_r}}\right)-1\right)\right), \quad \text{(A-9)}$$

with $\hat{p}_{11}\cdot\hat{n}=0, \hat{x}_{11}\cdot\hat{n}=0$, and

$$t(\mathbf{x},\mathbf{p_r}) = \tau(\mathbf{x},\mathbf{p_s}) + \mathbf{p_r}\cdot(\mathbf{r}-\boldsymbol{\xi}). \quad \text{(A-10)}$$

Using equations 13, 14, and A-8, we have

$$P(\mathbf{x},\omega) = -\omega^4 \iint \partial_n t(\mathbf{x},\mathbf{s})A(\mathbf{x},\mathbf{s})\partial_n t(\mathbf{x},\mathbf{p_r})A_r(\mathbf{x},\mathbf{p_r})d\mathbf{s}d\mathbf{p_r} \times \exp(i\omega(t(\mathbf{x},\mathbf{s})+\tau(\mathbf{x},\mathbf{p_r})-\mathbf{p_r}\cdot\boldsymbol{\xi})) \times \int P(\mathbf{s},\mathbf{r},\omega)\exp(i\omega\mathbf{p_r}\cdot\mathbf{r})d\mathbf{r}. \quad \text{(A-11)}$$

Taking into account equation 5, we get

$$P(\mathbf{x},\omega) = -\omega^4 \iint \partial_n t(\mathbf{x},\mathbf{s})A(\mathbf{x},\mathbf{s})\partial_n t(\mathbf{x},\mathbf{p_r})A_r(\mathbf{x},\mathbf{p_r}) \times \exp(i\omega(t(\mathbf{x},\mathbf{s})+\tau(\mathbf{x},\mathbf{p_r})-\mathbf{p_r}\cdot\boldsymbol{\xi}) \times P(\mathbf{s},\mathbf{p_r},\omega)d\mathbf{s}d\mathbf{p_r}. \quad \text{(A-12)}$$

Finally, ignoring the filter ω^4 and summing over all frequencies, we get

$$P(\mathbf{x}) = -\iint \partial_n t(\mathbf{x},\mathbf{s})A(\mathbf{x},\mathbf{s})\partial_n t(\mathbf{x},\mathbf{p_r})A_r(\mathbf{x},\mathbf{p_r}) \times P(\mathbf{s},\mathbf{p_r},t(\mathbf{x},\mathbf{s})+\tau(\mathbf{x},\mathbf{p_r})-\mathbf{p_r}\cdot\boldsymbol{\xi})d\mathbf{s}d\mathbf{p_r}. \quad \text{(A-13)}$$

If we now introduce

$$M(\mathbf{x},\mathbf{s},\mathbf{p_r}) = -A(\mathbf{x},\mathbf{s})A_r(\mathbf{x},\mathbf{p_r})\partial_n t(\mathbf{x},\mathbf{s})\partial_n t(\mathbf{x},\mathbf{p_r}),$$

then equation A-13 becomes

$$P(\mathbf{x}) = \iint M(\mathbf{x},\mathbf{s},\mathbf{p_r})P(\mathbf{s},\mathbf{p_r},t(\mathbf{x},\mathbf{s})+\tau(\mathbf{x},\mathbf{p_r})-\mathbf{p_r}\cdot\boldsymbol{\xi}) \times d\mathbf{s}d\mathbf{p_r}, \quad \text{(A-14)}$$

which is the receiver plane-wave imaging equation.

Source plane waves

Similarly, for the source plane-wave formulation, we use ART for the receiver Green's function and Chapman-Maslov formula for the source Green's function, and we get the source plane-wave imaging formula

$$P(\mathbf{x}) = \iint K(\mathbf{x},\mathbf{p_s},\mathbf{r})P(\mathbf{p_s},\mathbf{r},t(\mathbf{x},\mathbf{r})+\tau(\mathbf{x},\mathbf{p_s})-\mathbf{p_s}\cdot\boldsymbol{\xi}) \times d\mathbf{r}d\mathbf{p_s}, \quad \text{(A-15)}$$

where

$$K(\mathbf{x},\mathbf{p_s},\mathbf{r}) = -A_s(\mathbf{x},\mathbf{p_s})A(\mathbf{x},\mathbf{r})\partial_n t(\mathbf{x},\mathbf{p_s})\partial_n t(\mathbf{x},\mathbf{r}).$$

REFERENCES

Akbar, F. E., 1997, Three-dimensional prestack plane-wave Kirchhofff depth migration in laterally varying media: Ph.D. thesis, University of Texas at Austin.

Akbar, F. E., M. K. Sen, and P. L. Stoffa, 1996, Prestack plane-wave Kirchhoff migration in laterally varying media: Geophysics, **61**, 1068–1079.

Aminzadeh, F., J. Brac, and T. Kunz, 1997, 3-D salt and overthrust models: SEG/EAGE 3-D Modeling Series No. l, SEG.

Brysk, H., and D. W. McCowan, 1986, A slant-stack procedure for point-source data: Geophysics, **51**, 1370–1386.

Chapman, C. H., 2004, Fundamentals of seismic wave propagation: Cambridge University Press.

Chapman, C. H., and R. Drummond, 1982, Body-wave seismograms in inhomogeneous media using Maslov asymptotic theory: Bulletin of the Seismological Society of America, **72**, 277–317.

Claerbout, J. F., 1976, Fundamentals of geophysical data processing: McGraw-Hill Book Co. (A division of McGraw-Hill, Inc.).

———, 1985, Imaging the earth's interior: http://sepwww.stanford.edu/ftp/prof/.

Clayton, R. W., and R. H. Stolt, 1981, A Born-WKBJ inversion method for acoustic reflection data: Geophysics, **46**, 1559–1567.

Diebold, J. B., and P. L. Stoffa, 1981, The traveltime equation, tau-p mapping and inversion of common midpoint data: Geophysics, **46**, 238–254.

Faria, E. L., and P. L. Stoffa, 1994, Traveltime computation in transversely isotropic media: Geophysics, **59**, 272–281.

Farra, V., and P. Madariaga, 1987, Seismic waveform modeling in heterogeneous media by ray perturbation theory: Journal of Geophysical Research, **92**, 2697–2712.

Fokkema, J. T., and P. M. van den Berg, 1993, Seismic applications of acoustic reciprocity: Elsevier Science Publ. Co., Inc.

Foster, D. J., and C. C. Mosher, 1992, Suppression of multiple reflections using the Radon transform: Geophysics, **57**, 386–395.

Hildebrand, S. T., and R. J. Carroll, 1993, Radon depth migration: Geophysical Prospecting, **41**, 229–240.

Hill, N. R., 1990, Gaussian beam migration: Geophysics, **55**, 1416–1428.

Jiao, J., P. L. Stoffa, M. K. Sen, and R. K. Seifoullaev, 2002, Residual migration-velocity analysis in the plane-wave domain: Geophysics, **67**, 1252–1269.

Levander, A. R., 1988, Fourth-order finite-difference P-SV seismograms: Geophysics, **53**, 1425–1436.

Liu, F., M. K. Sen, and P. L. Stoffa, 2000, Dip selective 2-D multiple attenuation in the plane-wave domain: Geophysics, **65**, 264–274.

Liu, F., R. Stolt, D. Hanson, and R. Day, 2002, Plane wave source composition: An accurate phase encoding scheme for prestack migration: 72nd Annual International Meeting, SEG, Expanded Abstracts, 1156–1159.

McMechan, G. A., 1983, Migration by extrapolation of time-dependent boundary values: Geophysical Prospecting, **31**, 413–420.

Nowack, R. L., S. Dasgupta, and G. T. S. J. Sheng, 2006, Correlation migration using gaussian beams of scattered teleseismic body waves: Bulletin of the Seismological Society of America, **96**, 1–10.

Nowack, R. L., M. K. Sen, and P. L. Stoffa, 2003, Gaussian beam migration for sparse common-shot and common-receiver data: 73rd Annual International Meeting, SEG, Expanded Abstracts, 1114–1117.

Popov, M. M., 1982, A new method of computation of wave fields using Gaussian beams: Wave Motion, **4**, 85–97.

Romero, L. A., D. C. Ghiglia, C. C. Ober, and S. A. Morton, 2000, Phase encoding of shot records in prestack migration: Geophysics, **65**, 426–436.

Schneider, W. A., 1978, Integral formulation for migration in two-dimensions and three-dimensions: Geophysics, **43**, 49–76.

Schneider, W. A., K. A. Ranzinger, A. H. Balch, and C. Kruse, 1992, A dynamic programming approach to first arrival traveltime computation in media with arbitrarily distributed velocities: Geophysics, **57**, 39–50.

Schultz, P. S., and J. F. Claerbout, 1978, Velocity estimation and downward-continuation by wavefront synthesis: Geophysics, **43**, 691–714.

Sen, M. K., and L. N. Frazer, 1991, Multifold phase space path integral synthetic seismograms: Geophysical Journal International, **104**, 479–487.

Sen, M. K., and A. Mukherjee, 2003, τ-p analysis in transversely isotropic media: Geophysical Journal International, **154**, 647–658.

Sen, M. K., and P. L. Stoffa, 1991, Nonlinear one-dimensional seismic waveform inversion using simulated annealing: Geophysics, **56**, 1624–1638.
———, 1995, Global optimization methods in geophysical inversion: Elsevier Science Publ. Co. Inc.
Stoffa, P. L., ed., 1989, Tau-p: A plane wave approach to the analysis of seismic data: Kluwer Academic Publishers.
Stoffa, P. L., P. Buhl, J. B. Diebold, and F. Wenzel, 1981, Direct mapping of seismic data to the domain of intercept time and ray parameter — A plane-wave decomposition: Geophysics, **46**, 255–267.
Stoffa, P. L., M. K. Sen, R. K. Seifoullaev, R. Pestana, and J. T. Fokkema, 2005, Double plane wave kirchhoff depth migration: 9th International Congress of Brazilian Geophysical Society, Sociedade Brasileira de Geofisica, Extended Abstracts.
Stolt, R. H., 1978, Migration by Fourier transform: Geophysics, **43**, 23–48.
Stolt, R. H., and A. B. Weglein, 1985, Migration and inversion of seismic data: Geophysics, **50**, 2458–2472.
Tatalovic, R., M. W. P. Dillen, and J. T. Fokkema, 1991, Prestack imaging in the double transformed Radon domain: 61st Annual International Meeting, SEG, Expanded Abstracts, 1285–1288.
Tatham, R. H., 1989, Tau-p filtering, *in* P. L. Stoffa, ed., Tau-p: A plane wave approach to the analysis of seismic data: Kluwer Academic Publishers, 35–70.
Varela, C. L., P. L. Stoffa, and M. K. Sen, 1998, Background velocity estimation using non-linear optimization for reflection tomography and migration misfit: Geophysical Prospecting, **46**, 51–78.
Xia, G., M. K. Sen, and P. L. Stoffa, 1998, 1-D elastic waveform inversion: A divide-and-conquer approach: Geophysics, **63**, 1670–1684.
Xu, S., 1998, Maslov + Born migration/inversion in complex media: 68th Annual International Meeting, SEG, Expanded Abstracts, 1704–1707.
Zhang, Y., J. Sun, C. Notfors, S. Gray, L. Chernis, and J. Young, 2003, Delayed-shot 3D prestack depth migration: 73rd Annual International Meeting, SEG, Expanded Abstracts, 1027–1030.